

Inhibition of Skyrmion Hall Effect by a Stripe Domain Wall

Sheng Yang^{1,†}, Kai Wu,^{1,‡} Yuelei Zhao,^{1,‡} Xue Liang,¹ Jing Xia,² Yuqing Zhou,¹
Xiangjun Xing,^{3,*} and Yan Zhou^{1,†}

¹*School of Science and Engineering, The Chinese University of Hong Kong, Shenzhen 518172, China*

²*College of Physics and Electronic Engineering, Sichuan Normal University, Chengdu 610068, China*

³*School of Physics and Optoelectronic Engineering, Guangdong University of Technology, Guangzhou 510006, China*

(Received 27 December 2021; revised 27 April 2022; accepted 24 June 2022; published 10 August 2022)

Magnetic skyrmions are topologically protected particlelike spin textures initially discovered in chiral magnetic materials. When driven by an electric current, magnetic skyrmions move at a certain angle (i.e., skyrmion Hall angle) with respect to the driving current due to the Magnus force, giving rise to the so-called skyrmion Hall effect (SHE). The SHE often leads to skyrmion annihilation at the sample edge, which is detrimental for practical applications. In this work, we study, experimentally and through micromagnetic simulations, the current-driven dynamics of skyrmion bubbles (SBs) in Pt/Co/Ru multilayer stacks. It is observed that, under certain circumstances, a long stripe domain will form and align along the sample edge, which separates the skyrmion bubbles from the edge and avoids their annihilation at the edge. Furthermore, the velocity of the skyrmion bubbles can be increased by the stripe domain wall (DW) through the DW-SB interaction, as predicted in our early theory. Our results deepen our understanding of skyrmion dynamics and pave the way to the realization of highly efficient information processing and computing devices based on ultrafast skyrmion motion.

DOI: 10.1103/PhysRevApplied.18.024030

I. INTRODUCTION

Skyrmions are topological solitons with particlelike properties that exist ubiquitously in various systems, including bulk chiral magnets [1–4] and stacked multilayer thin films [5–11]. Recently, magnetic skyrmions have attracted lots of attention since they manifest emergent electrodynamics [12–17]. In particular, fast skyrmion motion can be induced by an applied electric current, which is highly promising for real applications, such as data storage and logic devices [18–23].

There are two major schemes to drive the skyrmions in magnetic thin films by electrical current: spin-transfer torque (STT) [15,24] and spin-orbit torque (SOT) [25,26]. These torques are both derived from the injected current. In magnetic thin-film systems, SOT is provided by heavy-metal layers; this is much stronger than STT. However, regardless of the STT or SOT, magnetic skyrmions experience the Magnus force, which leads to transverse motion of skyrmions relative to the current direction. This transverse motion is independent of the skyrmion size [27] and is

referred as the skyrmion Hall effect (SHE) [28–33], originating from the Berry phase [34,35]. As a result, magnetic skyrmions with high velocity eventually touch the edge of the sample and risk being annihilated.

Repulsion occurs when two topological domain walls (DWs) are close to each other [36,37]. It is reported that the interaction between a skyrmion and the device edge is repulsive [38,39]. Accordingly, the Magnus force on a skyrmion is likely to be balanced by the repulsive force; however, skyrmion annihilation at the edge is unavoidable once the skyrmion touches the edge. Consequently, a route to suppress the SHE without risking skyrmion annihilation requires urgent attention and attracts significant interest. Some researchers propose that an antiferromagnetic skyrmion or ferrimagnetic skyrmion at the compensation point would completely suppress the SHE [40–48]. It is also proposed that light-ion irradiation can be used to stabilize and guide the skyrmion on the track [49,50]. Distinct from device engineering [51–57], a promising approach is to guide skyrmion motion with a stripe domain wall [58,59]. For example, some of us predicted that the SHE could be suppressed alongside an elevated skyrmion velocity, which is ascribed to the exotic interaction between the skyrmions and stripe domain wall [58]. The study sheds light on potential zero-SHE schemes in skyrmionic device design and provides a theoretical guideline for our experimental implementation.

*xjxing@gdut.edu.cn

†zhouyan@cuhk.edu.cn

‡S. Yang, K. Wu, and Y. Zhao contributed equally to this work.

Here, we experimentally realize the SHE-free motion of skyrmion bubbles (SBs) at room temperature in a magnetic multilayer system. It is observed that, first, a long stripe domain is generated and aligned along an edge of the sample, and subsequently, the elongated domain wall is locally distorted by incident skyrmion bubbles and exerts a repulsive force on the skyrmion bubbles. Surprisingly, the edge stripe domain is very stable once it forms across the entire length of the sample. When the repulsive force and the Magnus force on the skyrmion reach an equilibrium, the transverse skyrmion motion is halted. Our experimental results validate our earlier theoretical predictions in Ref. [58].

II. EXPERIMENTAL METHODS

A. Sample preparation

The multilayer stack Ta(3)/[Pt(0.5)/Co(0.5)]₃/Ru(1.8)/[Co(0.5)/Pt(0.5)]₃/Ta(3) [thicknesses are in nanometers; see the inset in Fig. 1(a) for a cross-section view]

is deposited onto a Si substrate with a 300-nm-thick oxide layer at room temperature using a high-vacuum magnetron sputtering system (AJA International Inc.). The base pressure of the vacuum system is below 4×10^{-6} Pa. We optimize the thickness of the Ru layer to acquire the largest ferromagnetic coupling strength. Via lift-off photolithography, the multilayer is patterned to a 20- μm -wide device, which is attached to a homemade printed circuit board and bonded with electrodes for current injection (Keithley 6221 current source).

B. Measurement of current-driven motion

The hysteresis loop of the stack measured by the polar magneto-optic Kerr effect (MOKE) microscopy is shown in Fig. 1(a), which clearly indicates that the Co layers have a perpendicular magnetic anisotropy (PMA). The bottom Ta layer serves as a seed layer for the nucleation of top adlayers and also as a spin-current injector to generate

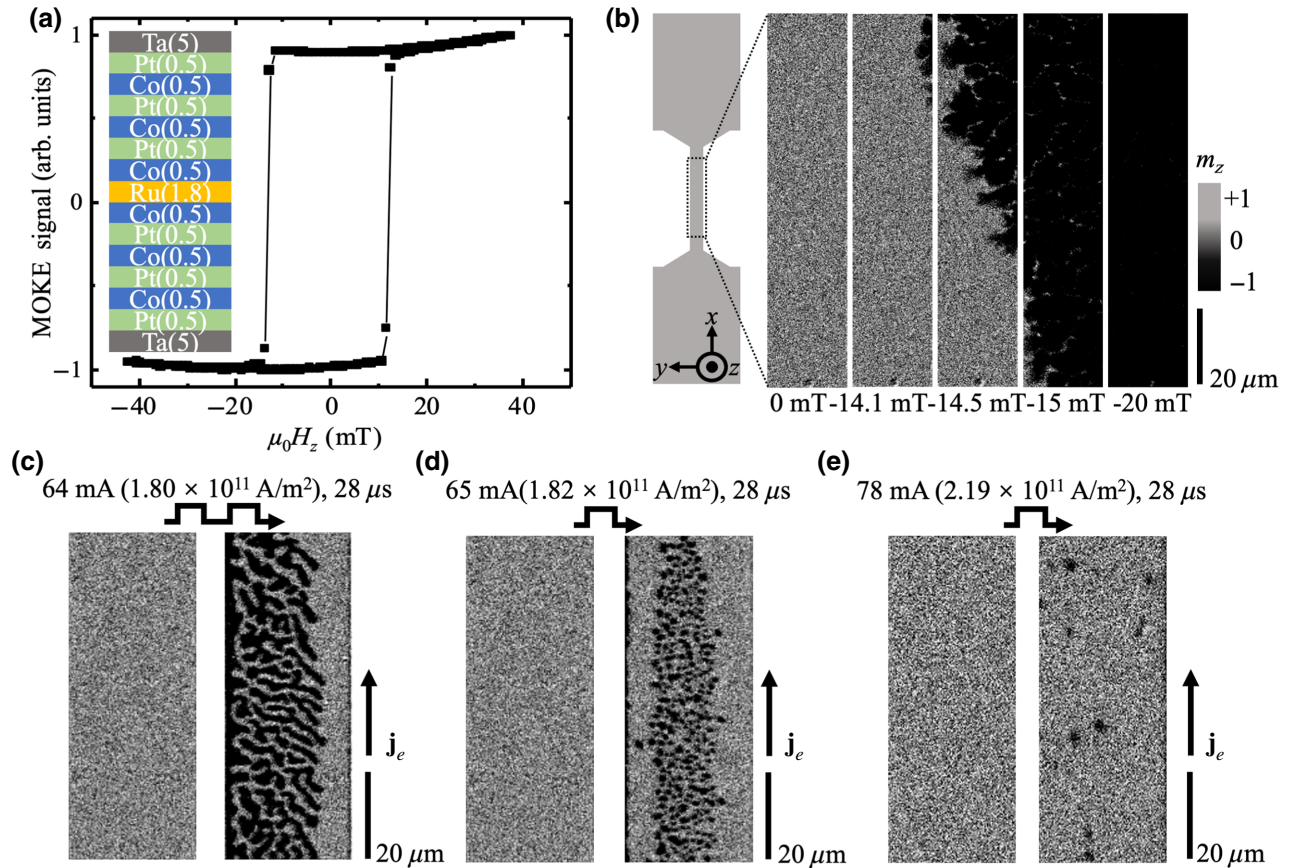


FIG. 1. Multilayer-stack magnetic thin film. (a) Optical hysteresis loop of the device with the Ta(5)/[Pt(0.5)/Co(0.5)]₃/Ru(1.8)/[Co(0.5)/Pt(0.5)]₃/Ta(5) stack structure is measured by polar MOKE, showing a coercivity of about ± 14 mT. Inset, cross section of the multilayer. (b) Evolution of magnetic domain patterns in out-of-plane external fields. Device is 20 μm in width and 120 μm in length. m_z is the z component of normalized magnetization. (c) Multiple 64-mA 28- μs sine pulses can generate stripe domains (see Video 1). (d) Single 65 mA with period of 28- μs sine pulse can generate skyrmion bubbles (see Video 2). (e) Creation of skyrmion bubbles by a single sine pulse with amplitude of 78 mA and period of 28 μs (see Video 3).

SOT for skyrmion-bubble manipulation [60–62]. To create skyrmion bubbles in our device, a single sine-wave current pulse with 28- μ s duration and 78-mA (current density of 2.2×10^{11} A/m²) amplitude is applied. Subsequently, square-wave current pulses, 10 μ s in duration and 84–86 mA (current density of 2.4×10^{11} A/m²) in amplitude, are used to manipulate the skyrmion bubbles. All the current densities are in the order of 10^{11} A/m². A MOKE microscope is used for direct imaging of the skyrmion bubbles.

C. Micromagnetic calculations

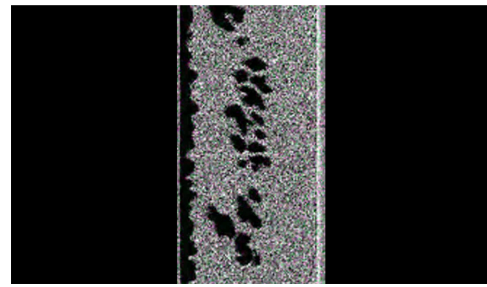
Here, we aim to reveal the impact of the interaction between the stripe domain walls and skyrmions bubbles on the dynamics of skyrmion bubbles. To the best of our knowledge, a quantitative description of the repulsive interaction remains elusive. In our experiment, the observed sizes of the skyrmion bubbles are several micrometers, in accordance with the measured weak Dzyaloshinskii-Moriya interaction (DMI) in our samples. Unfortunately, simulating such large skyrmions and even bigger magnetic samples (tens of micrometers) will result in an unacceptably long computation time. Thus, we adopt much smaller magnetic sample sizes in our simulations compared to the experiments. In order to adapt to the variation in the sample and skyrmion sizes, the values for some magnetic parameters used in the simulations might be different from the experimental values, as we resort to a qualitative, rather than quantitative analysis.

Micromagnetic modelling is carried out using the OOMMF code [63]. The numerical results are based on the following material parameters: saturation magnetization $M_s = 580$ kA/m, exchange stiffness $A = 15$ pJ/m, spin Hall angle $P = 0.4$, DMI strength $D = 4.0$ mJ/m², perpendicular magnetocrystalline anisotropy $K_u = 0.8$ MJ/m³, bias magnetic field $\mu_0 H_z = 50$ mT, and Gilbert damping constant $\alpha = 0.1$. The current density $J = 10$ MA/cm², model size $1000 \times 100 \times 1$ nm³, and mesh size $2 \times 2 \times 1$ nm³.

III. RESULTS AND DISCUSSION

A. Creation of skyrmion bubbles

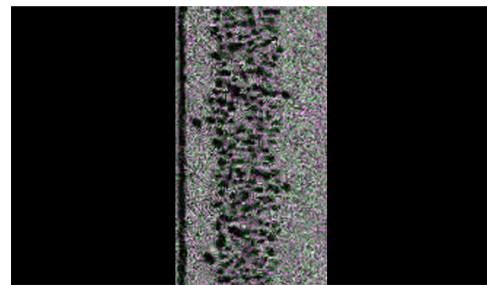
Figure 1(b) shows the layout of the sample and the typical domain patterns in out-of-plane magnetic fields, $\mu_0 H_z$, with certain strengths. The reverse labyrinthine domains begin to nucleate from the positive saturation state, when $\mu_0 H_z$ drops to -14.1 mT, and occupy the entire sample at -20 mT. According to the previous study, the labyrinthine domains can be converted into skyrmion bubbles [64]. Our multilayer stack embodies a weak DMI due to the broken inversion symmetry at the Pt/Co interface. The effective DMI field is $\mu_0 H_{\text{DMI}} = 10$ mT, as reflected in the shift of the out-of-plane hysteresis loops under different dc currents and in-plane bias fields [65].



VIDEO 1. Multiple 64-mA 28- μ s sine pulses can generate stripe domains.

Despite numerous alternative methods to create and manipulate skyrmions (e.g., spin waves [66], heat [67], and electric field [68]), skyrmion creation based on electric currents remains appealing because of its complementary metal oxide semiconductor (CMOS) compatibility and capability of on-chip integration. Hence, skyrmion creation and manipulation via electric currents are extensively addressed [69,70].

As shown in Fig. 1(c) (see Video 1) and Fig. 1(d) (see Video 2), the minimum current to generate skyrmion bubbles in our experiments is a single 65-mA sinusoidal pulse with a pulse width of 28 μ s. However, if we reduce the current amplitude to 64 mA with a duration of 28 μ s, it is impossible to generate any skyrmion bubbles, even if we apply hundreds of wave pulses to the device, as shown in Fig. 1(e). Multiple 64-mA pulses generate more heat than a single 65-mA pulse, which indicates that the thermal effect is not responsible for skyrmion-bubble creation. Instead of skyrmion bubbles, these multiple 64-mA pulses with a duration of 28 μ s create a series of stripe domains [see Fig. 1(c)]. We optimize the generation conditions and demonstrate skyrmion-bubble creation in the Pt/Co/Ru sample in Fig. 1(e) (see Video 3). To favor the creation of skyrmion bubbles, we first apply an external field, $\mu_0 H_z$, of +200 mT to fully magnetize the device. Next, $\mu_0 H_z$ is decreased to 0.4 mT, which proves to be the optimal value. To initialize creation, a single sine-wave current pulse with 28- μ s duration and 78-mA amplitude is injected



VIDEO 2. Single 65-mA sine pulse with period of 28 μ s can generate skyrmion bubbles.

into the sample along $+x$. Figure 1(e) demonstrates the successful creation of skyrmion bubbles about $0.5 \mu\text{m}$ in diameter across the device, as a result of the concerted action of SOT and heat. A pulse with a width of $28 \mu\text{s}$ can also cause Joule heating to accumulate. However, the heat assists only SOT to overcome the pinning-energy barrier to generate skyrmion bubbles. In principle, the stabilization of skyrmion bubbles arises from the trade-off among the exchange, dipolar, PMA, DMI, and Zeeman energy and interactions. In addition, the stray field also plays a role in stabilizing skyrmion bubbles in addition to the DMI in our sample.

B. Current-driven skyrmion motion

The corresponding results are shown in Figs. 2(a)–2(g). Attached at the top of each MOKE image is the count

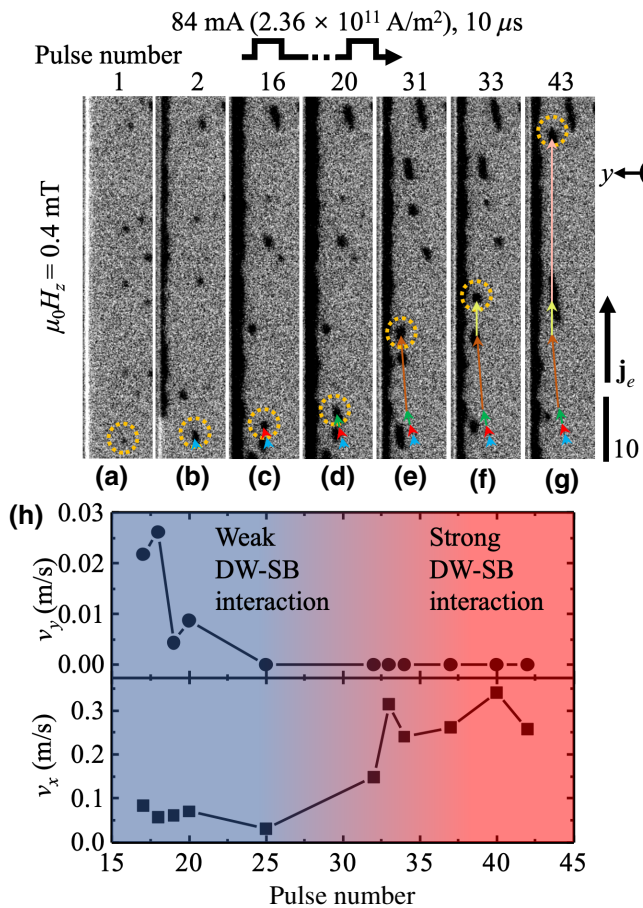
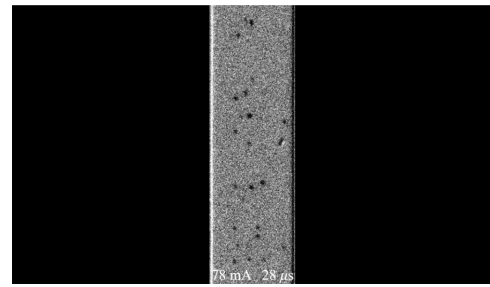
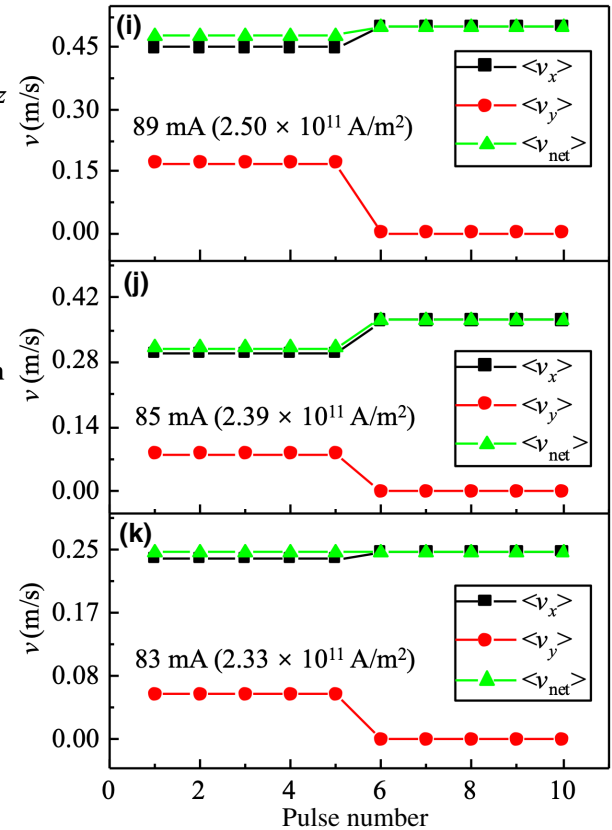


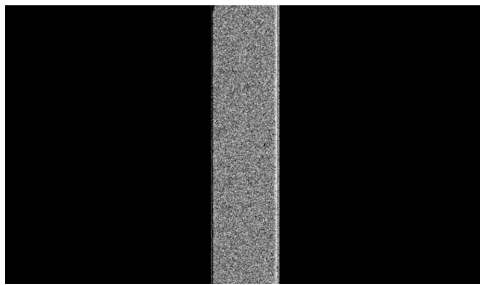
FIG. 2. Current-driven skyrmion motion. (a)–(g) Sequence of MOKE images of the skyrmion bubble (circled in yellow) driven by electron-current pulses. Pulse count is labeled at the top of each MOKE image. Pulse 1 is imposed right after the creation of skyrmion bubbles. Pulses 2–43 are sequential 84-mA (current density of $2.36 \times 10^{11} \text{ A/m}^2$) 10- μs square-wave pulses. Electron current is along $+x$ (see Video 9 for (a)–(d) and Video 10 for (e)–(g) [77]). Sample is positively saturated, and all the experiments are performed under an external field of $\mu_0 H_z = 0.4 \text{ mT}$. (h) Skyrmion velocity as a function of pulse count. (i)–(k) Velocity increase contributed by the DW-SB interactions. Average velocity without the DW-SB interaction is shown for pulses 1–5, while the average velocity with the DW-SB interaction is shown for pulses 6–10. Here, 10- μs square-wave pulses are used [see Video 11 for (i), Video 12 for (j), and Video 13 (k)].



VIDEO 3. Creation of skyrmion bubbles by a single sine pulse with amplitude of 78 mA and period of 28 μs .

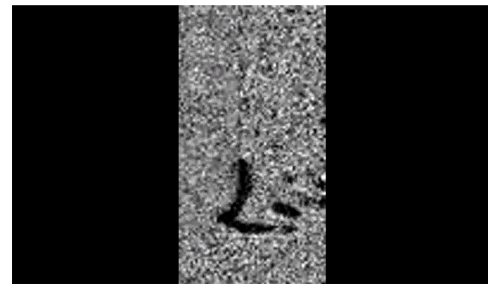
of the pulses supplied to the device. While SOT provides the main driving force for the motion of skyrmion bubbles, we believe that the thermal effect of the current pulse also helps to overcome the pinning barrier of the sample.





VIDEO 4. No skyrmion bubbles can be created by the motion-driving pulses (multiple 84 mA, 10- μ s square-wave pulses).

Microsecond-range pulses of current can cause heat to accumulate. Some researchers have reported that the pure SOT pulses in the nanosecond range are sufficient to nucleate skyrmions [71–74]. However, in our sample, we find that the pinning is much stronger than that in other typical skyrmion samples. Therefore, we need a higher energy or current than in a typical skyrmion sample to overcome the pinning-energy barrier (see Video 4). In other words, heat can act as a catalyst to help the SOT drive skyrmion bubbles in the nanowires; however, large current can cause the deformation of skyrmion bubbles (See Appendix A and Video 16). Pulse 1 [Fig. 2(a)] is applied to the device immediately after bubble creation, as mentioned in the preceding section. On the action of pulse 2 [Fig. 2(b)], the skyrmion bubble (circled in yellow) shifts, as denoted by the blue arrow, and meanwhile, the skyrmion bubble expands, showing a size of about 1 μ m. In the meantime, a stripe domain is nucleated around the left edge and eventually fills almost the entire length of the sample. In our experiments, the stripe domain is spontaneously formed at one edge of the sample via expansion and merging of the seed domains. Generally, it is thought that the random defects in the sample are disadvantageous due to the pinning effect. However, in our experiments, these randomly distributed point impurities play a crucial role in the formation of the edge-stripe domains. The reverse domains are easier to form at these locations and require less energy.



VIDEO 6. Some skyrmion bubbles nucleate around the corner underneath the electrode.

These impurities provide the conditions for the creation of the seed domains with reverse magnetization. Most commonly, the skyrmion bubbles created in the interior are converted into the reverse domains after colliding with the sample edge due to the SHE (see Video 5). In the skyrmion-bubble creation process, some skyrmion bubbles nucleate around the corner underneath the electrode (see Video 6), where the greatly reduced current density is insufficient to shift these skyrmion bubbles but sufficiently large to elongate them along the edge (see Video 7). In this way, such elongated skyrmion bubbles function as reverse domains. Occasionally, *in situ* nucleation of seed reverse domains on the edge can be observed, which occurs alongside the nucleation of reverse labyrinthine domains in the interior (see Video 8).

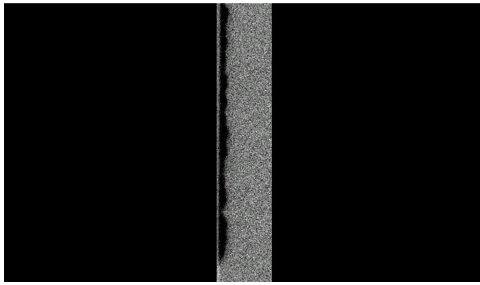
Before the 14th pulse, the skyrmion bubble is pinned at a position, probably due to the randomly distributed defects, whereas the stripe domain spreads across the full length of the sample. The red arrow in Fig. 2(c) indicates the displacement of the skyrmion bubble from the pinning site. When the skyrmion bubble is far from the stripe domain, a weak or even vanishing DW-SB interaction is expected, and the repulsive force experienced by the skyrmion bubble does not suffice to cancel out the Magnus force. In Fig. 2(d), the trajectory of the skyrmion bubble from pulse 1 to pulse 20, as marked by the joint arrows in different colors, is clearly indicative of the SHE.



VIDEO 5. Skyrmion bubbles created in the interior convert to the reverse domains after colliding with the sample edge due to the SHE.



VIDEO 7. Domain close to the electrode is elongated along the edge under stimulation by the pulses.

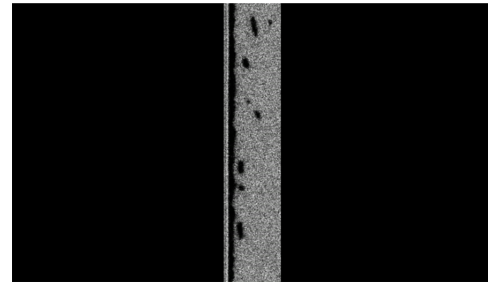


VIDEO 8. *In situ* nucleation of seed reverse domains on the edge.

As the skyrmion bubble deflects further, the DW-SB interaction continues to be strengthened. After pulse 20 [Fig. 2(d)], the skyrmion bubble's trajectory becomes nearly parallel to the edge, implying that the DW-SB repulsion is strong enough to suppress the SHE. In particular, as shown in Fig. 2(g), after pulse 31, the skyrmion bubble's trajectories (denoted by the light-yellow and light-pink arrows) follow the current direction, suggesting that the Magnus force and the repulsive force experienced by the skyrmion bubble equal each other.

According to Figs. 2(a)–2(g), repeated applications of current pulses result in a constant DW-SB separation, and thus, in a considerable DW-SB repulsion. Namely, the strength of the DW-SB interaction is associated with the pulse count. Figure 2(h) shows the skyrmion-bubble-velocity evolution with the pulse count. It is seen that the transverse velocity (v_y) vanishes in the strong DW-SB interaction regime, implying a balance between the repulsive and Magnus forces. In the weak DW-SB interaction regime (see Video 9), the longitudinal velocity of the skyrmion bubble fluctuates around an average value $\langle v_x \rangle = 0.07$ m/s, and the transverse velocity continually falls from $\langle v_y \rangle = 0.016$ m/s to zero, because of the gradually increasing repulsive force. Based on the initial velocities, the skyrmion Hall angle is about 12°.

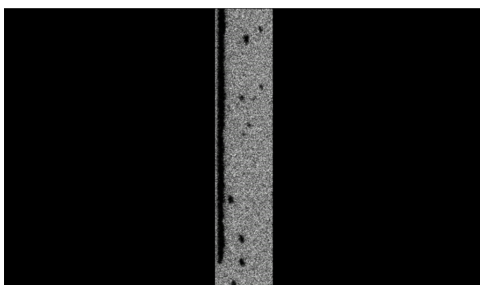
In the strong DW-SB interaction regime (see Video 10), v_y is always zero, and thereby, the total average velocity is $\langle v_x \rangle = 0.24$ m/s, approximately twice as large as that



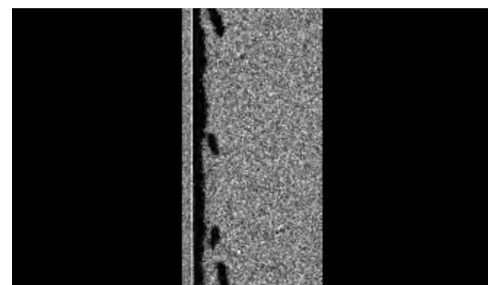
VIDEO 10. Current-driven skyrmion motion after encountering the DW-SB interaction.

in the weak DW-SB interaction regime. The net velocity increase can be observed at different current amplitudes. Figures 2(i) and 2(j) show the average velocity variation. Note that the velocities for pulses 1 to 5 are the average velocities without the DW-SB interaction, and the velocities for pulses 6 to 10 are the average velocities with the DW-SB interaction. The average net velocity increases from 0.48 to 0.5 m/s with a pulse amplitude of 89 mA [Fig. 2(i), see Video 11] and from 0.31 to 0.37 m/s with a pulse amplitude of 85 mA [Fig. 2(j), see Video 12]. No apparently accessible net velocity change is observed at a current magnitude of 83 mA [Fig. 2(k), see Video 13]. The increase in the skyrmion-bubble velocity agrees with the prediction by our earlier theory [58], which revealed that, when the skyrmion interacted with a domain wall, the domain wall underwent an asymmetric distortion and imposed a repulsive force (F_p) on the skyrmion bubble. Because of the asymmetric distortion of the domain wall, the repulsive force incorporates two in-plane components: F_{\parallel} and F_{\perp} , which are parallel and perpendicular to the current direction, respectively. In our experiments, F_{\parallel} directly leads to the increased longitudinal velocity of the skyrmion bubble.

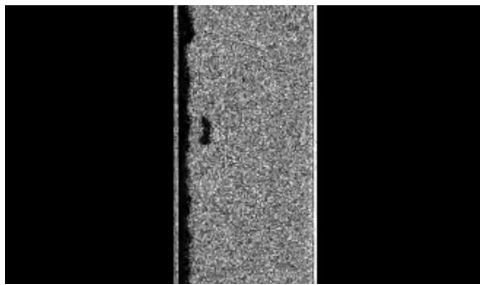
The local distortion of the domain wall is remarkable upon the application of the current. In our experiments, a pulse rather than continuous dc current is used to drive the skyrmion bubble, so the domain wall is intermittently distorted and the system relaxes freely and the distortion



VIDEO 9. Current-driven skyrmion motion before encountering the DW-SB interaction.



VIDEO 11. More examples of velocity increases [corresponding to Fig. 2(i)].

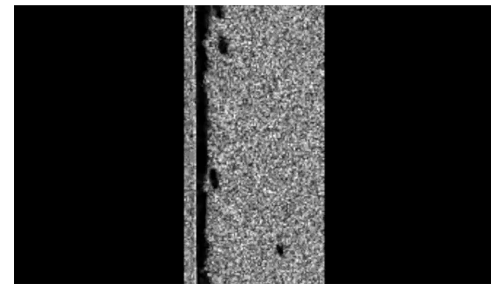


VIDEO 12. More examples of velocity increases [corresponding to Fig. 2(j)].

is restored during the delay. As a consequence, we cannot directly identify the dynamic distortion of the stripe domain wall because of the low temporal resolution of our MOKE microscope.

C. Simulation of current-driven skyrmion motion

The current-driven skyrmion motion is simulated using OOMMF [63]. Figure 3(b) depicts the skyrmion-bubble dynamics in the nanowire harboring a stripe domain. Initially, a skyrmion is placed in the nanowire, which accompanies the long stripe domain attached to the left edge of the nanowire. At 0 ns, an electron current along $+x$ is applied to the nanowire. Afterwards, the skyrmion proceeds at an angle with respect to the current direction. As a result, the stripe domain wall distorts and the skyrmion shrinks. Specifically, at 1.0 ns, one can see a local dip in the stripe domain beside the skyrmion with a reduced diameter. Soon, the system arrives at a dynamic equilibrium, so that, as time elapses, one cannot distinguish a variation in the local magnetization structure (compare the images at 2.0, 3.0, and 4.0 ns). Once attaining equilibrium,



VIDEO 13. More examples of velocity increases [corresponding to Fig. 2(k)].

the skyrmion bubble moves at a constant speed under the guidance of the stripe domain wall.

For comparison, the skyrmion-bubble dynamics without including a stripe domain is presented in Fig. 3(a). At 0 ns, an electron current along $+x$ is applied to the nanowire hosting a skyrmion. Driven by the current, the skyrmion moves forward and simultaneously gets close to the edge exhibiting the SHE; 2 ns later, the skyrmion touches the edge of the nanowire. Soon afterwards, the skyrmion is destroyed and ultimately vanishes.

We would like to point out that assuming a big DMI in the simulations does not qualitatively change the results, which are valid irrespective of the DMI strength, as long as the Néel configuration is maintained.

D. Skyrmion-bubble depinning from a trap

In our experiments, we observe a process in which the skyrmion bubble escapes from a trap, as illustrated in Fig. 4 (see Video 14). We believe this phenomenon can provide further evidence to support our conclusion. The electron-current pulses (amplitude 86 mA, duration 10 μ s,

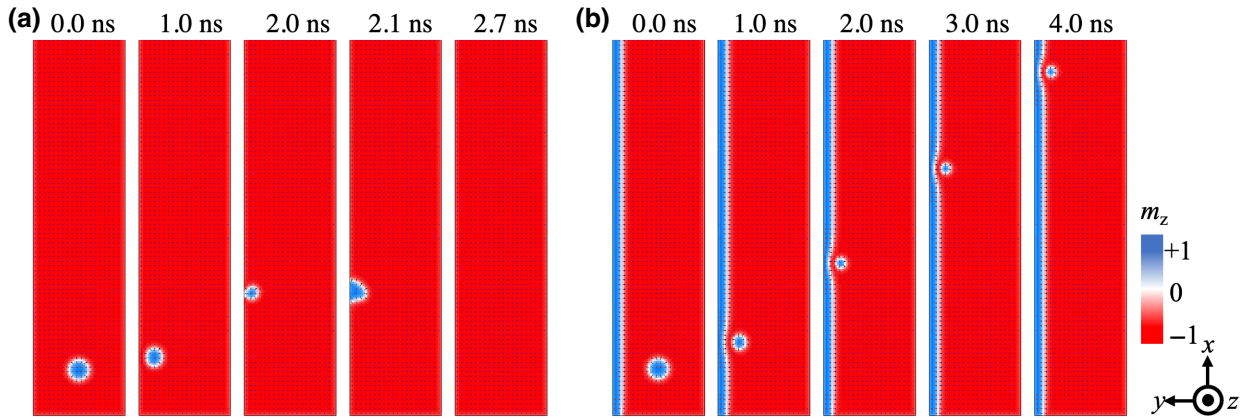


FIG. 3. OOMMF simulation results of skyrmion motion. (a) Skyrmion motion along a nanowire without inclusion of a stripe domain wall. (b) Skyrmion motion along a nanowire including a stripe domain wall. Electron current is along $+x$ and current density is $J = 10 \text{ MA}/\text{cm}^2$. Time elapsed from current onset is indicated at the top of each panel. Sample size is $1000 \times 100 \times 1 \text{ nm}^3$ and the mesh size is $2 \times 2 \times 1 \text{ nm}^3$.

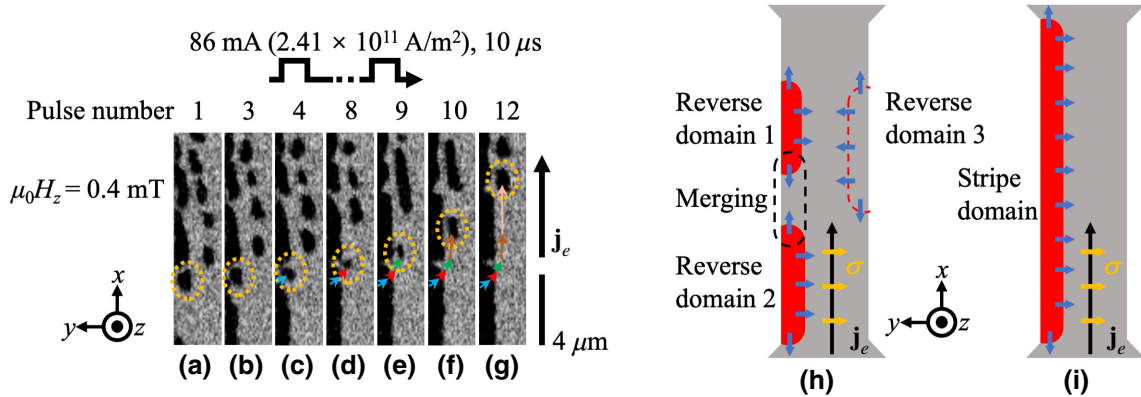


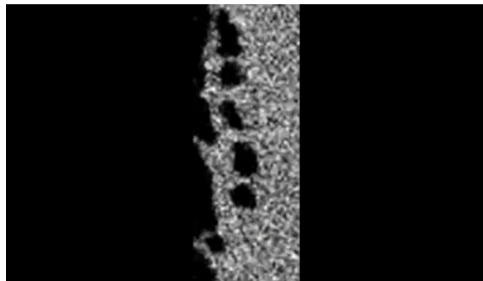
FIG. 4. Stripe-domain formation and skyrmion-bubble depinning. (a)–(g) Escape process of a skyrmion bubble from a trapping potential. Square-wave-pulse amplitudes and durations are 86 mA (current density of $2.41 \times 10^{11} \text{ A/m}^2$) and 10 μs , respectively. Electron current is along $+x$ (see Video 15). (h),(i) Mechanism of stripe-domain formation. Under SOT, reverse domains 1 and 2 will merge when their caps contact, and reverse domain 3 will be split apart and vanish, leaving a stripe domain on the left edge.

square-wave pulse) are injected into the device along $+x$. Figure 4(a) (pulse 1) shows a trapped skyrmion bubble (circled in yellow) and some capped stripe domains inhabiting the sample edge. In an ideal scenario, the skyrmion bubble is anticipated to move under the driving current. However, as shown in Fig. 4(a), a domain cap lies in front of the skyrmion bubble and traps it by virtue of the DW-SB repulsion, which cancels out the current's driving force on the skyrmion bubble.

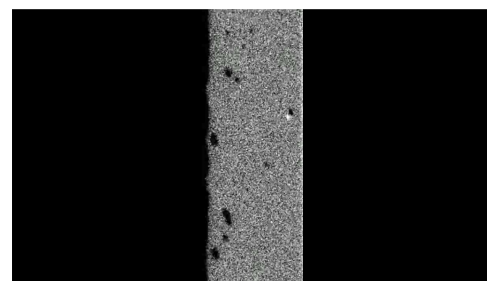
As shown in Fig. 4(b), on applying pulse 3, a new stripe domain appears at the lower terminal of the sample and elongates upwards, approaching the upper stripe domain. Triggered by pulse 4, the upper and lower stripe domains merge at their caps and become a single stripe domain containing a dip, as shown in Figs. 4(c)–4(g). Under the continual action of subsequent pulses, the valley on the stripe domain wall lifts gradually. As the distance between the valley and the skyrmion bubble decreases, the skyrmion bubble experiences an increasing repulsive force along $-y$. In this way, the skyrmion bubble escapes from the trapping potential.

The arrows in Figs. 4(c)–4(g) mark the displacements of the skyrmion bubble, which jointly show the trajectory of the skyrmion bubble. Initially, DW-SB repulsion on the skyrmion bubble surpasses the Magnus force, leading to a transverse velocity of the skyrmion bubble [Figs. 4(c)–4(e)], which vanishes when the two forces equilibrate [Figs. 4(f) and 4(g)]. From Figs. 4(e) and 4(f), the skyrmion bubble is seen to expand, which is attributable to random point defects widely existing in Pt/Co. Pinned by the point defects, a skyrmion bubble cannot shift as a whole but will expand under the action of the SOT. In fact, the stripe domains originate from the expansion of small reverse domains formed at the sample edge, where the random defects usually pin some portion of a reverse domain. Driven by the SOT, the reverse domains expand along the edge via the cap motion and ultimately coalesce into a stripe domain, for which the mechanism is elucidated in Refs. [75,76].

In our experiments, the stripe domain forms only at one edge of the sample, as shown in Figs. 2(a)–2(g) and 4(a)–4(g) (see Video 15). This originates from correct



VIDEO 14. Escaping process of a skyrmion bubble from a trapping potential.



VIDEO 15. Full device view for current-driven skyrmion motion.

matching between the magnetization direction on the stripe domain wall and the polarization direction of the injected spin current. Assuming that, initially, seed reverse domains nucleate at both edges of the sample, one will immediately find that the domain walls at opposite edges have antiparallel magnetization orientations (along $\pm y$), as shown in Fig. 4(h), because of a fixed chirality. The polarization direction of the spin current, $\sigma = \hat{z} \times \hat{\mathbf{j}}$ ($\hat{\mathbf{j}}$ denotes a unit vector along the electric current), is always along $-y$ [Fig. 4(h)]. Hence, for the stripe domain wall on the left edge, the magnetization, $\mathbf{m} \parallel \sigma$, leads to a vanishing SOT ($\tau_{SO} \sim \mathbf{m} \times \sigma \times \mathbf{m}$). Whereas for the stripe domain wall on the right edge, $\mathbf{m} \parallel -\sigma$, in which a considerable SOT will arise once the magnetization on the wall deviates from the equilibrium orientation ($+y$) due to, e.g., thermal fluctuation or pinning. Under SOT, the seed reverse domain on the right edge will immediately deform and be annihilated, since the SOT tends to align \mathbf{m} (along $+y$) in the direction of σ (along $-y$). Ultimately, no stripe domains inhabit the right edge of the sample [Fig. 4(i)]. Intriguingly, the domain wall at the left edge is stabilized by the SOT, because the SOT will drive magnetization on the wall to restore the equilibrium orientation in case of a slight deviation. Meanwhile, the two caps of a seed reverse domain undergo a finite SOT, and thus, move along the edge when the SOT overcomes the pinning potential. Under appropriate conditions, neighboring reverse domains (reverse domains 1 and 2) merge into a single stripe domain, as shown in Figs. 4(h) and 4(i).

The DW-SB interaction can significantly affect the behavior of the skyrmion bubble, and depending on the interaction strength, the skyrmion bubble exhibits distinct dynamics. Figures 2(a)–2(d) shows that the Magnus force dominates the skyrmion transverse motion in the weak DW-SB interaction regime. However, once the skyrmion bubble enters the strong DW-SB interaction regime, the Magnus force will be equilibrated and the skyrmion bubble has no transverse motion, as shown in Figs. 2(e)–2(g). In the case of a zero Magnus force, the DW-SB repulsion serves to depin the skyrmion bubble from a trap.

IV. CONCLUSION

We study, experimentally and through micromagnetic simulations, the dynamics of skyrmion bubbles and stripe domain walls driven by current pulses. Our results demonstrate that the edge-stripe domain can form spontaneously at one edge of the sample, and the stripe domain wall helps depin a skyrmion bubble and enhance the motion of the skyrmion bubble via suppressing the SHE. Guided by the stripe domain wall, the skyrmion bubble moves along the current direction at an elevated velocity without risking annihilation at the edge. In our scheme, the

SHE is circumvented without introducing complex circuits and magnetic structure redesign. These findings will help surmount critical technical obstacles met in the development of skyrmionic devices and magnonic fibers.

ACKNOWLEDGMENTS

This work is supported by the Guangdong Special Support Project (Grant No. 2019BT02X030), the Guangdong Basic and Applied Basic Research Foundation (Grant No. 2021B1515120047), the Shenzhen Fundamental Research Fund (Grant No. JCYJ20210324120213037), the Shenzhen Peacock Group Plan (Grant No. KQTD20180413181702403), the Pearl River Recruitment Program of Talents (Grant No. 2017GC010293), and the National Natural Science Foundation of China (Grant Nos. 11974298 and 61961136006). X.X. acknowledges support by the National Natural Science Foundation of China (Grant No. 11774069) and support by the Guangdong Provincial Natural Science Foundation of China (Grant No. 2022A1515010605). Y.L.Z. acknowledges support by the National Natural Science Foundation of China (Grant No. 12004319). J.X. acknowledges support by the National Natural Science Foundation of China (Grant No. 12104327).

The manuscript was written through contributions of all authors. All authors have given approval to the final version of the manuscript.

The authors declare no competing interests.

APPENDIX A: SKYRMION-BUBBLE DEFORMATION UNDER LARGE CURRENT

In our study, the optimal current-driven skyrmion-bubble current conditions are square-wave pulses of 82–92 mA with a pulse width of 10 μ s. Larger currents can easily cause the device to burn out after tens of pulses. However, we still find that the skyrmion bubbles and edge-stripe domains are disrupted or transformed once we apply large currents (Fig. 5).

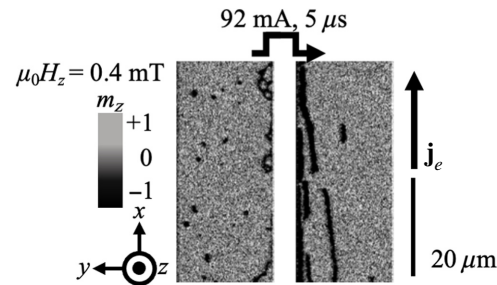
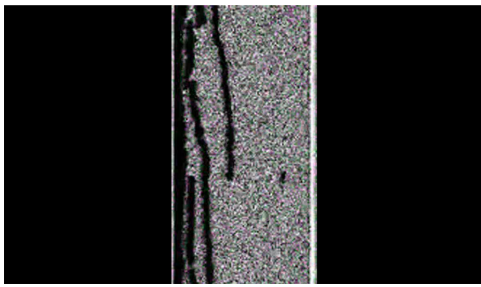


FIG. 5. The 92-mA ($3.28 \times 10^{11} \text{ A/m}^2$) 5- μ s square pulses can cause the deformation of skyrmion bubbles (see Video 16).



VIDEO 16. The 92-mA 5- μ s square pulses can cause the deformation of skyrmion bubbles.

- [1] K. Karube, J. S. White, D. Morikawa, M. Bartkowiak, A. Kikkawa, Y. Tokunaga, T. Arima, H. M. Rønnow, Y. Tokura, and Y. Taguchi, Skyrmion formation in a bulk chiral magnet at zero magnetic field and above room temperature, *Phys. Rev. Mater.* **1**, 074405 (2017).
- [2] S. L. Zhang, G. van der Laan, W. W. Wang, A. A. Haghigirad, and T. Hesjedal, Direct Observation of Twisted Surface Skyrmions in Bulk Crystals, *Phys. Rev. Lett.* **120**, 227202 (2018).
- [3] M. T. Birch, D. Cortés-Ortuño, L. A. Turnbull, M. N. Wilson, F. Groß, N. Träger, A. Laurenson, N. Bukin, S.H. Moody, M. Weigand, and G. Schütz, Real-space imaging of confined magnetic skyrmion tubes, *Nat. Commun.* **11**, 1726 (2020).
- [4] Y. Fujima, N. Abe, Y. Tokunaga, and T. Arima, Thermodynamically stable skyrmion lattice at low temperatures in a bulk crystal of lacunar spinel GaV₄Se₈, *Phys. Rev. B* **95**, 180410(R) (2017).
- [5] Z. Qin, Y. Wang, S. Zhu, C. Jin, J. Fu, Q. Liu, and J. Cao, Stabilization and reversal of skyrmion lattice in Ta/CoFeB/MgO multilayers, *ACS Appl. Mater. Interfaces* **10**, 36556 (2018).
- [6] Z. Qin, C. Jin, H. Xie, X. Li, Y. Wang, J. Cao, and Q. Liu, Size-tunable skyrmion bubbles in Ta/CoFeB/MgO multilayers, *J. Phys. D: Appl. Phys.* **51**, 425001 (2018).
- [7] B. Ojha, S. Mallick, S. K. Panigrahy, M. Sharma, A. Thiaville, S. Rohart, and S. Bedanta, Driving skyrmions with low threshold current density in Pt/CoFeB thin film, *arXiv:2106.02407*.
- [8] S. Woo, K. Litzius, B. Krüger, M.-Y. Im, L. Caretta, K. Richter, M. Mann, A. Krone, R. M. Reeve, and M. Weigand, *et al.*, Observation of room-temperature magnetic skyrmions and their current-driven dynamics in ultrathin metallic ferromagnets, *Nat. Mater.* **11**, 501 (2016).
- [9] C. Moreau-Luchaire, C. Moutafis, N. Reyren, J. Sampaio, C. A. F. Vaz, N. Van Horne, K. Bouzehouane, K. Garcia, C. Deranlot, and P. Wernicke, *et al.*, Additive interfacial chiral interaction in multilayers for stabilization of small individual skyrmions at room temperature, *Nat. Nanotechnol.* **11**, 444 (2016).
- [10] O. Boulle, J. Vogel, H. Yang, and S. Pizzini, Room-temperature chiral magnetic skyrmions in ultrathin magnetic nanostructures, *Nat. Nanotechnol.* **11**, 449 (2016).

- [11] R. Wiesendanger, Nanoscale magnetic skyrmions in metallic films and multilayers: A new twist for spintronics, *Nat. Rev. Mater.* **1**, 1 (2016).
- [12] Y. Zhou, Magnetic skyrmions: Intriguing physics and new spintronic device concepts, *Natl. Sci. Rev.* **6**, 210 (2019).
- [13] N. Nagaosa and Y. Tokura, Topological properties and dynamics of magnetic skyrmions, *Nat. Nanotechnol.* **8**, 899 (2013).
- [14] G. Yu, P. Upadhyaya, Q. Shao, H. Wu, G. Yin, X. Li, C. He, W. Jiang, X. Han, and P. K. Amiri, *et al.*, Room-temperature skyrmion shift device for memory application, *Nano Lett.* **17**, 261 (2017).
- [15] S. Komineas and N. Papanicolaou, Skyrmion dynamics in chiral ferromagnets, *Phys. Rev. B* **92**, 064412 (2015).
- [16] A. Hrabec, J. Sampaio, M. Belmeguenai, I. Gross, R. Weil, S. M. Chérif, A. Stashkevich, V. Jacques, A. Thiaville, and S. Rohart, Current-induced skyrmion generation and dynamics in symmetric bilayers, *Nat. Commun.* **8**, 15765 (2017).
- [17] M. Schott, A. Bernand-Mantel, L. Ranno, S. Pizzini, J. Vogel, H. Béa, C. Baraduc, S. Auffret, G. Gaudin, and D. Givord, The skyrmion switch: Turning magnetic skyrmion bubbles *on* and *off* with an electric field, *Nano. Lett.* **17**, 3006 (2017).
- [18] X. Zhang, M. Ezawa, and Y. Zhou, Magnetic skyrmion logic gates: Conversion, duplication and merging of skyrmions, *Sci. Rep.* **5**, 9400 (2015).
- [19] A. Fert, N. Reyren, and V. Cros, Magnetic skyrmions: Advances in physics and potential applications, *Nat. Rev. Mater.* **210**, 17031 (2017).
- [20] S. Luo, M. Song, X. Li, Y. Zhang, J. Hong, X. Yang, X. Zou, N. Xu, and L. You, Reconfigurable skyrmion logic gates, *Nano Lett.* **18**, 1180 (2018).
- [21] Y. Huang, W. Kang, X. Zhang, Y. Zhou, and W. Zhao, Magnetic skyrmion-based synaptic devices, *Nanotechnology* **28**, 08LT02 (2017).
- [22] Z. R. Yan, Y. Z. Liu, Y. Guang, K. Yue, J. F. Feng, R. K. Lake, G. Q. Yu, and X. F. Han, Skyrmion-Based Programmable Logic Device with Complete Boolean Logic Functions, *Phys. Rev. Appl.* **15**, 064004 (2021).
- [23] D. Pinna, F. Abreu Araujo, J.-V. Kim, V. Cros, D. Querlioz, P. Bessiere, J. Droulez, and J. Grollier, Skyrmion Gas Manipulation for Probabilistic Computing, *Phys. Rev. Appl.* **9**, 064018 (2018).
- [24] J. Masell, D. R. Rodrigues, B. F. McKeever, and K. Everschor-Sitte, Spin-transfer torque driven motion, deformation, and instabilities of magnetic skyrmions at high currents, *Phys. Rev. B* **101**, 214428 (2020).
- [25] S. Woo, K. M. Song, H.-S. Han, M.-S. Jung, M.-Y. Im, K.-S. Lee, K. S. Song, P. Fischer, J.-I. Hong, J. W. Choi, *et al.*, Spin-orbit torque-driven skyrmion dynamics revealed by time-resolved x-ray microscopy, *Nat. Commun.* **8**, 15573 (2017).
- [26] G. Yu, P. Upadhyaya, X. Li, W. Li, S. K. Kim, Y. Fan, K. L. Wong, Y. Tserkovnyak, P. K. Amiri, and K. L. Wang, Room-temperature creation and spin-orbit torque manipulation of skyrmions in thin films with engineered asymmetry, *Nano Lett.* **16**, 1981 (2016).
- [27] K. Zeissler, S. Finizio, C. Barton, A. J. Huxtable, J. Massey, J. Raabe, A. V. Sadovnikov, S. A. Nikitov, R. Brearton, T. Hesjedal, *et al.*, Diameter-independent skyrmion hall angle

- observed in chiral magnetic multilayers, *Nat. Commun.* **11**, 428 (2020).
- [28] C. Reichhardt and C. J. Olson Reichhardt, Noise fluctuations and drive dependence of the skyrmion Hall effect in disordered systems, *New J. Phys.* **18**, 095005 (2016).
- [29] J. Zang, M. Mostovoy, J. H. Han, and N. Nagaosa, Dynamics of Skyrmion Crystals in Metallic Thin Films, *Phys. Rev. Lett.* **107**, 136804 (2011).
- [30] W. Jiang, X. Zhang, G. Yu, W. Zhang, X. Wang, M. Benjamin Jungfleisch, J. E. Pearson, X. Cheng, O. Heinonen, and K. L. Wang, *et al.*, Direct observation of the skyrmion Hall effect, *Nat. Phys.* **13**, 162 (2017).
- [31] K. Litzius, I. Lemesh, B. Krüger, P. Bassirian, L. Caretta, K. Richter, F. Büttner, K. Sato, O. A. Tretiakov, and J. Förster, *et al.*, Skyrmion Hall effect revealed by direct time-resolved x-ray microscopy, *Nat. Phys.* **13**, 170 (2017).
- [32] R. Juge, S.G. Je, D. de Souza Chaves, L.D. Budapejbeanu, J. Peña-Garcia, J. Nath, I.M. Miron, K.G. Rana, L. Aballe, and M. Foerster, *et al.*, Current-Driven Skyrmion Dynamics and Drive-Dependent Skyrmion Hall Effect in an Ultrathin Film, *Phys. Rev. Appl.* **12**, 044007 (2019).
- [33] B. L. Brown, U. C. Täuber, and M. Pleimling, Effect of the Magnus force on skyrmion relaxation dynamics, *Phys. Rev. B* **97**, 020405(R) (2018).
- [34] H. Kurebayashi, J. Sinova, D. Fang, A. C. Irvine, T. D. Skinner, J. Wunderlich, V. Novák, R. P. Campion, B. L. Gallagher, E. K. Vehstedt, *et al.*, An antidamping spin-orbit torque originating from the Berry curvature, *Nat. Nanotechnol.* **9**, 211 (2014).
- [35] J. Ye, Y. B. Kim, A. J. Millis, B. I. Shraiman, P. Majumdar, and Z. Tešanović, Berry Phase Theory of the Anomalous Hall Effect: Application to Colossal Magnetoresistance Manganites, *Phys. Rev. Lett.* **83**, 3737 (1999).
- [36] L. Thomas, M. Hayashi, R. Moriya, C. Rettner, and S. Parkin, Topological repulsion between domain walls in magnetic nanowires leading to the formation of bound states, *Nat. Commun.* **3**, 810 (2012).
- [37] C. Jin, J. Wang, W. Wang, C. Song, J. Wang, H. Xia, and Q. Liu, Array of Synchronized Nano-Oscillators Based on Repulsion between Domain Wall and Skyrmion, *Phys. Rev. Appl.* **9**, 044007 (2018).
- [38] X. Zhang, G. P. Zhao, H. Fangohr, J. P. Liu, W. X. Xia, J. Xia, and F. J. Morvan, Skyrmion-skyrmion and skyrmion-edge repulsions in skyrmion-based racetrack memory, *Sci. Rep.* **5**, 7643 (2015).
- [39] J. C. Martinez, W. S. Lew, W. L. Gan, and M. B. A. Jalil, Theory of current-induced skyrmion dynamics close to a boundary, *J. Magn. Magn. Mater.* **465**, 685 (2018).
- [40] S. Woo, K. M. Song, X. Zhang, Y. Zhou, M. Ezawa, X. Liu, S. Finizio, J. Raabe, N. J. Lee, and S.-I. Kim, *et al.*, Current-driven dynamics and inhibition of the skyrmion Hall effect of ferrimagnetic skyrmions in GdFeCo films, *Nat. Commun.* **9**, 959 (2018).
- [41] T. Dohi, S. DuttaGupta, S. Fukami, and H. Ohno, Formation and current-induced motion of synthetic antiferromagnetic skyrmion bubbles, *Nat. Commun.* **10**, 5153 (2019).
- [42] X. Zhang, Y. Zhou, and M. Ezawa, Antiferromagnetic skyrmion: Stability, creation and manipulation, *Sci. Rep.* **6**, 24795 (2016).
- [43] P. Siegl, M. Stier, A. F. Schäffer, E. Y. Vedmedenko, T. Posske, R. Wiesendanger, and M. Thorwart, Creating arbitrary sequences of mobile magnetic skyrmions and antiskyrmions, *ArXiv:2111.03007 [Cond-Mat]* (2021).
- [44] Y. Hirata, D.-H. Kim, S. K. Kim, D.-K. Lee, S.-H. Oh, D.-Y. Kim, T. Nishimura, T. Okuno, Y. Futakawa, and H. Yoshikawa, *et al.*, Vanishing skyrmion Hall effect at the angular momentum compensation temperature of a ferrimagnet, *Nat. Nanotechnol.* **14**, 232 (2019).
- [45] H. Wu, F. Groß, B. Dai, D. Lujan, S. A. Razavi, P. Zhang, Y. Liu, K. Sobotkiewich, J. Förster, and M. Weigand, *et al.*, Ferrimagnetic skyrmions in topological insulator/ferrimagnet heterostructures, *Adv. Mater.* **32**, 2003380 (2020).
- [46] X. Zhang, Y. Zhou, and M. Ezawa, Magnetic bilayer-skyrmions without skyrmion Hall effect, *Nat. Commun.* **7**, 10293 (2016).
- [47] Y. Zhang, S. Luo, B. Yan, J. Ou-Yang, X. Yang, S. Chen, B. Zhu, and L. You, Magnetic skyrmions without the skyrmion Hall effect in a magnetic nanotrack with perpendicular anisotropy, *Nanoscale* **9**, 10212 (2017).
- [48] S. K. Kim, K. Nakata, D. Loss, and Y. Tserkovnyak, Tunable magnonic thermal Hall effect in skyrmion crystal phases of ferrimagnets, *Phys. Rev. Lett.* **122**, 057204 (2019).
- [49] R. Juge, K. Bairagi, K. G. Rana, J. Vogel, M. Sall, D. Mailly, V. T. Pham, Q. Zhang, N. Sisodia, M. Foerster, *et al.*, Helium ions put magnetic skyrmions on the track, *Nano Lett.* **21**, 2989 (2021).
- [50] L.-M. Kern, B. Pfau, V. Deinhart, M. Schneider, C. Klose, K. Gerlinger, S. Wittrock, D. Engel, I. Will, and C.M. Günther, *et al.*, Deterministic generation and guided motion of magnetic skyrmions by focused He⁺-ion irradiation, *Nano Lett.* **22**, 4028 (2022).
- [51] K. Ohara, X. Zhang, Y. Chen, Z. Wei, Y. Ma, J. Xia, Y. Zhou, and X. Liu, Confinement and protection of skyrmions by patterns of modified magnetic properties, *Nano Lett.* **21**, 4320 (2021).
- [52] B. Göbel, A. Mook, J. Henk, and I. Mertig, Overcoming the speed limit in skyrmion racetrack devices by suppressing the skyrmion Hall effect, *Phys. Rev. B* **99**, 020405(R) (2019).
- [53] D. Toscano, J. P. A. Mendonça, A. L. S. Miranda, C. I. L. de Araujo, F. Sato, P. Z. Coura, and S. A. Leonel, Suppression of the skyrmion Hall effect in planar nanomagnets by the magnetic properties engineering: Skyrmion transport on nanotacks with magnetic strips, *J. Magn. Magn. Mater.* **504**, 166655 (2020).
- [54] J. Yang, K.-W. Moon, A. M. G. Park, S. Lee, D. H. Kang, M. Shin, S. Kim, and K.-J. Kim, Racetrack memory based on current-induced motion of topological Bloch lines, *Appl. Phys. Express* **14**, 103002 (2021).
- [55] P. Lai, G. P. Zhao, H. Tang, N. Ran, S. Q. Wu, J. Xia, X. Zhang, and Y. Zhou, An improved racetrack structure for transporting a skyrmion, *Sci. Rep.* **7**, 45330 (2017).
- [56] X. Wang, W. L. Gan, J. C. Martinez, F. N. Tan, M. B. A. Jalil, and W. S. Lew, Efficient skyrmion transport mediated by a voltage controlled magnetic anisotropy gradient, *Nanoscale* **10**, 733 (2018).

- [57] I. Purnama, W. L. Gan, D. W. Wong, and W. S. Lew, Guided current-induced skyrmion motion in 1D potential well, *Sci. Rep.* **5**, 10620 (2015).
- [58] X. Xing, J. Åkerman, and Y. Zhou, Enhanced skyrmion motion via strip domain wall, *Phys. Rev. B* **101**, 214432 (2020).
- [59] M. Song, K.-W. Moon, S. Yang, C. Hwang, and K.-J. Kim, Guiding of dynamic skyrmions using chiral magnetic domain wall, *Appl. Phys. Express* **13**, 063002 (2020).
- [60] A. Manchon and S. Zhang, Theory of spin torque due to spin-orbit coupling, *Phys. Rev. B* **79**, 094422 (2009).
- [61] P. M. Haney and M. D. Stiles, Current-Induced Torques in the Presence of Spin-Orbit Coupling, *Phys. Rev. Lett.* **105**, 126602 (2010).
- [62] J. Sinova, S. O. Valenzuela, J. Wunderlich, C. H. Back, and T. Jungwirth, Spin Hall effects, *Rev. Mod. Phys.* **87**, 1213 (2015).
- [63] M. J. Donahue and D. G. Porter, OOMMF User's Guide, v. 1.0 (National Institute of Standards and Technology, Gaithersburg, MD, 1999); NIST Interagency Report No. NISTIR6376, 1999.
- [64] W. Jiang, P. Upadhyaya, W. Zhang, G. Yu, M. B. Jungfleisch, F. Y. Fradin, J. E. Pearson, Y. Tserkovnyak, K. L. Wang, and O. Heinonen, *et al.*, Blowing magnetic skyrmion bubbles, *Science* **349**, 283 (2015).
- [65] C.-F. Pai, M. Mann, A. J. Tan, and G. S. D. Beach, Determination of spin torque efficiencies in heterostructures with perpendicular magnetic anisotropy, *Phys. Rev. B* **93**, 144409 (2016).
- [66] Y. Liu, G. Yin, J. Zang, J. Shi, and R. K. Lake, Skyrmion Creation and Annihilation by Spin Waves, *Appl. Phys. Lett.* **107**, 152411 (2015).
- [67] W. Koshibae and N. Nagaosa, Creation of skyrmions and antiskyrmions by local heating, *Nat. Commun.* **5**, 5148 (2014).
- [68] P. Huang, M. Cantoni, A. Kruchkov, J. Rajeswari, A. Magrez, F. Carbone, and H. M. Rønnow, *In situ* electric field skyrmion creation in magnetoelectric Cu₂ OSeO₃, *Nano Lett.* **18**, 5167 (2018).
- [69] H. Y. Yuan and X. R. Wang, Skyrmion creation and manipulation by nano-second current pulses, *Sci. Rep.* **6**, 22638 (2016).
- [70] Y. Tchoe and J. H. Han, Skyrmion generation by current, *Phys. Rev. B* **85**, 174416 (2012).
- [71] S. Finizio, K. Zeissler, S. Wintz, S. Mayr, T. Weßels, A. J. Huxtable, G. Burnell, C. H. Marrows, and J. Raabe, Deterministic field-free skyrmion nucleation at a nanoengineered injector device, *Nano Lett.* **19**, 7246 (2019).
- [72] F. Büttner, I. Lemesh, M. Schneider, B. Pfau, C. M. Günther, P. Hessing, J. Geilhufe, L. Caretta, D. Engel, B. Krüger, *et al.*, Field-free deterministic ultrafast creation of magnetic skyrmions by spin-orbit torques, *Nat. Nanotechnol.* **12**, 1040 (2017).
- [73] M. Baumgartner, K. Garello, J. Mendil, C. O. Avci, E. Grimaldi, C. Murer, J. Feng, M. Gabureac, C. Stamm, Y. Acremann, *et al.*, Spatially and time-resolved magnetization dynamics driven by spin-orbit torques, *Nat. Nanotechnol.* **12**, 980 (2017).
- [74] S. Woo, K. M. Song, X. Zhang, M. Ezawa, Y. Zhou, X. Liu, M. Weigand, S. Finizio, J. Raabe, M.-C. Park, *et al.*, Deterministic creation and deletion of a single magnetic skyrmion observed by direct time-resolved x-ray microscopy, *Nat. Electron.* **1**, 288 (2018).
- [75] X. Xing, P. W. T. Pong, and Y. Zhou, Current-controlled unidirectional edge-meron motion, *J. Appl. Phys.* **120**, 203903 (2016).
- [76] X. Xing, P. W. T. Pong, J. Åkerman, and Y. Zhou, Paving Spin-Wave Fibers in Magnonic Nanocircuits Using Spin-Orbit Torque, *Phys. Rev. Appl.* **7**, 054016 (2017).